Northumbria Research Link

Generalized Modeling of Origami Folding Joints

Hongying Zhang, Huijuan Feng, Jian-Lin Huang, Jamie Paik[*]

*Corresponding author. Jamie Paik is with the Reconfigurable Robotics Laboratory, École Polytechnique Fédérale de Lausanne (EPFL), 1015 Lausanne, Switzerland. Email: Jamie.paik@epfl.ch.

Abstract

Origami robots self-reconfigure from a two-dimensional manufactured state to three-dimensional mobile robots. By folding, they excel in transforming their initial spatial configuration to expand their functionalities. However, unlike paper-based origamis, where the materials can remain homogeneous, origami robots require high payloads and controllability of their reconfigurations. Therefore, the mechanisms to achieve automated folding adopt thick panels and folding hinges that are often of different materials. While the fundamental working principle of origami hinges remains simple, these multi-material origami joints can no longer be modeled by beam theory without considering the semi-rigid connections at the material interfaces. Currently, there is no comprehensive model to analyze the physical behavior of an actuated folding hinge accurately. In this work, we propose a plate theory-based model to analyze the origami folding joints: we adapt a torsional spring to capture the semi-rigid connection, predict the folding stiffness and deflection of folding hinges. Herein, the semi-rigid connection is calibrated by quasi-static folding tests on a series of origami folding joints, and the accuracy of our model is compared to finite element simulations. With this analytical model, we can accurately simulate the mechanics of physical origami folding joints.

Key words

Physical origami, Origami folding joint, Mechanics modeling

1. Introduction

The origami principle of folding two-dimensional sheets into three-dimensional structures can lead to both beautiful artwork and practical robotic solutions (1-6). Therefore, they are shifting the paradigm in design, fabrication, and perception of autonomous mesoscale robots (7-10). The origami folding joints are fundamental components that enable both build-in compliance and movability of the robot. To ensure the functionality of physical origami robots, they are structured as thick panels and foldable hinges that are made of various engineering materials (2-5,11,12). This is the major difference from the models of zero-thickness sheets and zero-width creases as in traditional paper-based origamis (13-16). Therefore, the rotational pin-joint like folding behavior is obtained by the localized bending of the folding hinges. The folding hinge together with its adjacent thick panels is defined as an origami folding joint in this paper (Fig. 1A). The nonzero-width hinges are often built by thin sheets and typical applications can be found in pneumatic (4,17, 18) and magnetic (19-22) actuated origami robots, cable-driven manipulators (15,23), buckling-triggered bistable origami structures (24-26), and origami metamaterials (27-32). In recent years, researchers are adopting active materials, e.g. shape memory alloy or polymers (3, 33-36), electromagnetic polymers (20), or photic material (37-40), which allows a series of origami robots to self-fold or self-assemble.

For all folding robots, the folding flexible hinges bend locally to exert rotation on their adjacent thick panels. In this manner, the folding hinge induces stiffness, stores elastic energy, and exhibits high-order geometric continuity during the localized bending. To evaluate the elastic energy stored in origami folding joints, the hinges are often modeled as torsional

springs whose stiffness is roughly estimated by beam theory as described in Fig. 1B (5, 26). By definition of beam theory, folding hinges are simplified to one-dimensional (1D) line (41), even though its lateral dimension is much larger than the principle bending dimension. Considering the geometry, a folding hinge is a natural thin plate that undergoes two-dimensional (2D) deformation. However, the 1D simplification of beam model fails to capture this 2D deformation. Moreover, the beam model only applies to small deformation, while the folding hinges normally undergo a large deformation to enable the folding in an origami structure. Recently, researchers adopt plate model to simulate the mechanics of folding hinges (42,43). However, these initial works are empirical because they roughly model the deflection as a ruling surface, whose parametric curve is approximated by a polynomial curve. To capture the localized bending at folding hinges, researchers also use finite element analysis (FEA) to model the bending region with shell elements but at high computational cost (30, 40). Therefore, we need an analytical model that can accurately capture the large deflection and physical folding stiffness of the folding hinges.

Most origami robots are fabricated by lamination method (3,5,22,35) or multimaterial 3D printing technique (20,37,44), which bonds or merges thick panels and folding hinges by melting or photocuring the structural materials. Delamination failure frequently happens at the material interface between the thick panels and folding hinges, indicating that the connection is not rigidly bonded or plastic deformation is yielded. Until now, no research has covered this semi-rigid connection behavior. To accurately predict the mechanical property of origami folding joints, we indeed need a model that incorporates this semi-rigid behavior.

In this work, we present for the first time a model to analyze the mechanics of origami folding joints accurately. This new amelioration of origami folding joint model allows origami robots to be reliably modelled for control by considering the behavior of inhomogeneous materials construction and semi-rigid connection. As denoted in Fig. 1C, we model the hinge as a thin plate, the semi-rigid connection as torsional springs. The crucial challenge lies in how to explicitly describe the constraints of a folding joint, and solve its deflection function under all these constraints. Herein, the hinges of these origami joints are modeled as elastically supported thin plates (45-47). To calibrate the semi-rigid connection, we prepare a series of origami joints and conducted quasi-static folding tests. Comparison with FEA simulations on two origami joint prototypes, the analytical model achieves high accuracy in predicting the mechanics of origami joints. With the analytical model and experimentally calibrated semi-rigid index, one can predict the folding stiffness of any origami folding joint of the same materials and fabrication technique.
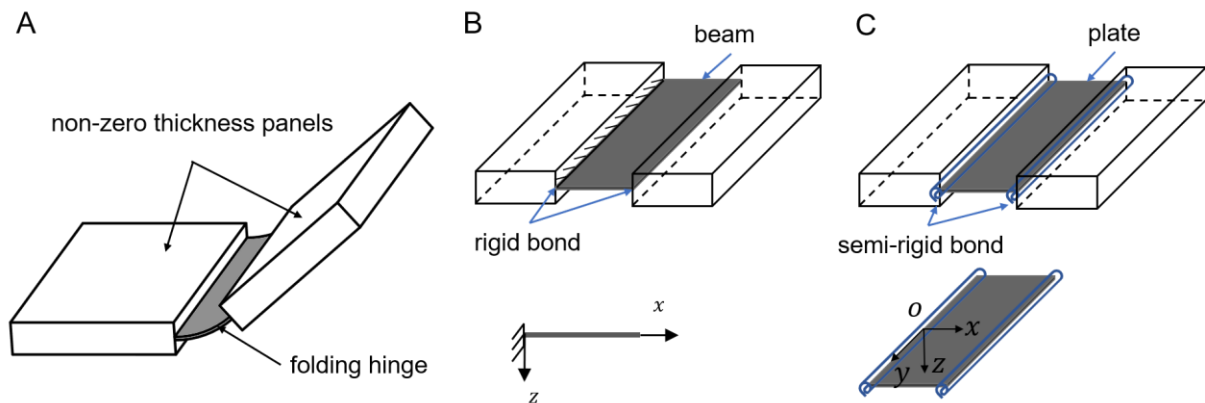
Fig. 1 Diagram of an origami folding joint. *(A) An origami folding joint is composed of two thick panels and a folding hinge. (B) Until now, the hinge is roughly modeled as a cantilever beam clamped to adjacent panels. (C) In this work, the hinge is accurately modeled as an elastically supported thin plate.*

2. Modeling of origami folding joints

To model the localized bending at the folding hinges, the first challenge is converting physical working conditions into explicit constraints. After, the critical difficulty is solving the deflection function that satisfies both the complicated constraints and equilibrium requirements. As shown in Fig. 2A, the hinge is taken as a thin plate of width, $2a$, length, l, and thickness, h, held at $x=0$, actuated upon by a uniformly distributed force P or moment M at $x=l$ and free of stress along the edges $y=\pm a$. Reissner released a general form of the deflection function (48),

$$w = \frac{1}{D(1-v)}\left(-\frac{C}{6}x^3 + \frac{B}{2}x^2\right) + \frac{v}{D(1-v)}\frac{y^2}{2}(Cx - B) + \frac{F}{D}x + \frac{I}{D} \tag{1}$$

The details of the analysis are provided in Supplementary S1. Here, $C, B, F,$ and I are four integration constants, determined by the boundary and loading conditions; D is the flexural rigidity of the plate, relating to the material's Young's modulus, E, Poisson's ratio, v, and thickness, h, determined by

$$D = \frac{Eh^3}{12(1-v^2)}. \tag{2}$$

The bending moment, M_x, twisting moments, M_{xy}, shear force, Q_x, and bending angle, φ_x shown in Fig. 2A can be obtained by substituting the deflection function w into their expressions denoted in Supplementary S1. Their expressions are:

$$M_x = (1+v)(Cx - B), \tag{3a}$$

$$M_{xy} = vCy - Ak\sinh\frac{y}{k}, \tag{3b}$$

$$Q_x = C + A\cosh\frac{y}{k}, \tag{3c}$$

$$\varphi_x = -\frac{1}{D}\left[\frac{1}{1-v}\left(-\frac{C}{2}x^2 + Bx\right) + \frac{Cv}{1-v}\frac{y^2}{2} + F\right] + \frac{12(1+v)}{5Eh}\left(C + A\cosh\frac{y}{k}\right). \tag{3d}$$

Here, A is also an integration constant determined by constraints, and $k^2 = h^2/10$ as defined in Supplementary S1.
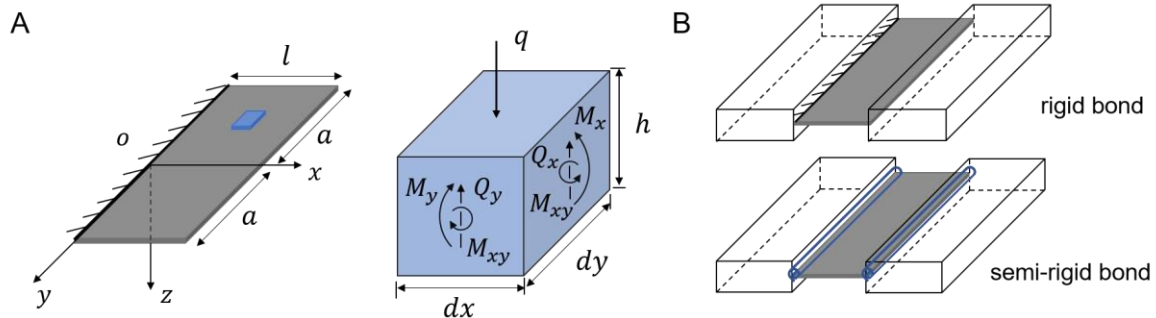
Fig. 2 Two bonding conditions for origami folding joint. *(A)The folding hinge is molded as a cantilever plate with the directions of moments and stresses shown on an infinitesimal element. (B) In this work, we analyze two prototypes of origami folding joints, namely rigid bond and semi-rigid bond.*

In this work, we extend the preliminary work on the cantilever plate to model the localized bending at the folding hinges of origami folding joints. Rather than directly clamping at the edges, two parallel edges of the hinges are rigidly joined to two torsional springs (Fig. 1C). To obtain the deflection of origami hinges, we derive the explicit boundary conditions for the semi-rigid connection, then solve the corresponding integration constants. Herein, we simulate a rigidly bonded origami folding joint as a reference. To be noted, we focus on the deflection of folding hinge and rotation of the loaded panel in the physical origami joint. In this manner, all possible configurations of origami folding joints are analysed, and the effects of a semi-rigid connection are explicitly investigated.

2.1 Rigid bond origami folding joints

An origami folding joint may be actuated by pure transverse force, moment, or hybrid. Considering the hybrid loading condition is equivalent to a superpose of individual loads, we focus on pure loads. Regarding the rigid bond origami joint in Fig. 3A, its hinge is ideally bonded to the adjacent thick panels. Therefore, the hinge is modeled as a cantilever plate clamped at $x = 0$, actuated by distributed transverse force P or moment M on $x = l$, and free of stress on $y = \pm a$. Its boundary and loading conditions are expressed explicitly as follows

$$w = \varphi_x = 0 \text{ for } x = 0, \tag{4a}$$

$$M_x = 0, \int_{-a}^{a} Q_x dy = P \text{ for } x = l, \tag{4b-1}$$

$$M_x = M, \int_{-a}^{a} Q_x dy = 0 \text{ for } x = l, \tag{4b-2}$$

$$M_{xy} = 0 \text{ for } y = \pm a, \tag{4c}$$

where Eq. 4a describes the deflection and rotation constraints on edge $x = 0$; Eq. 4b denotes the loading condition on edge $x = l$, in which Eq. 4b-1 prescribes a transverse force P-loaded plate and Eq. 4b-2 indicates a moment M case; and Eq. 4c reveals no shearing moment on the free edges $y = \pm a$. Considering the constraints on M_y, Q_x, q are already incorporated in deriving Eq. 1 (see Supplementary S1), so they are not restated here.

In previous work (48), Eq. 4a is assumed merely to satisfy at the origin. However, this assumption is true only the length over width ratio $(l/2a)$ of a plate is relatively high. For a folding hinge, its $l/2a$ ratio is extremely low, and the assumption leads to a saddle-shaped deflection surface, which contradicts the physical deformation. Therefore, the constraints in Eq. 4q must be satisfied on the whole edge $x = 0$. By substituting the expressions of w, φ_x into Eq. 4a, we can obtain

$$\left(w \right)_{x=0} = -\frac{vB}{2D(1-v)} y^2 + \frac{I}{D} = 0, \tag{5a}$$

$$\left(\varphi_x \right)_{x=0} = -\frac{vC}{2D(1-v)} y^2 - \frac{F}{D} + \frac{12(1+v)}{5Eh} \left(C + A \cosh \frac{y}{k} \right) = 0. \tag{5b}$$

To solve the integration constants, we introduce a trigonometric cosine expansion to approximate Eq. 5 as functions of y within the region $[-a, a]$. Afterward, we group the terms

containing $\cos\left[(m\pi y)/2a\right]$, where m are odd integers, and set their coefficients equal to zero because Eq. 5 holds for all y within the design domain (details in Supplementary S2). Following this process, the integration constants I and F are computed as :

$$I = \frac{2a^2 vB}{(1-v)} \sum_{m=1,3,5,\ldots}^{\infty} \left[\frac{1}{m\pi} - \left(\frac{2}{m\pi}\right)^3\right](-1)^{\frac{m-1}{2}} \cos\frac{m\pi y}{2a},$$

$$F = \frac{h^2 C}{5(1-v)} - \sum_{m=1,3,5,\ldots}^{\infty} \left\{\frac{2Cva^2}{1-v}\left[\frac{1}{m\pi} - \left(\frac{2}{m\pi}\right)^3\right] + \frac{4h^2 A}{5m\pi(1-v)}\frac{\cosh\frac{a}{k}}{1+\left(\frac{2a}{km\pi}\right)^2}\right\}(-1)^{\frac{m-1}{2}} \cos\frac{m\pi y}{2a}.$$

$$(6)$$

Substituting moments M_x, M_{xy}, and shearing force Q_x from Eq. 3 into Eq. 4b-1 and Eq. 4c, we obtain the integration constants $A, B,$ and C for a hinge under terminal force, P :

$$A = \frac{vP}{2(1+v)k\sinh\frac{a}{k}}, B = \frac{Pl}{2(1+v)a}, C = \frac{P}{2(1+v)a}.$$

$$(7)$$

Substituting the integration constants in Eq. 6 and Eq. 7 into Eq. 1, we can obtain the deflection function for a rigid-bond origami folding joint under terminal force, P. Specifically, if the length, l of the hinge is far more than its width, a, the deflection w is simplified to:

$$w = \frac{P}{2aD(1-v^2)}\left[-\frac{x^3}{6} + \frac{lx^2}{2} + \frac{v}{2}(x-l)y^2 + 2k^2 x\left(1 + \frac{av}{k\sinh\frac{a}{k}}\right)\right].$$

$$(8)$$

which is consistent with the result in (48). An origami folding joint normally undergoes large folding; therefore, it is critical to capture the deformed position of $x=l$, marked as l'. The neutral surface of the folding hinge is unstretched under the terminal force P, thus any strip parallel to the x-axis maintains its original length. To simplify the computational process, we take the strip $y=0$ to compute the deformed position of the right edge $x=l'$:

$$\int_0^{l'}\sqrt{1 + \frac{P^2}{4a^2 D^2(1-v^2)^2}\left[-\frac{1}{2}x^2 + lx + 2k^2\left(1 + \frac{av}{k\sinh\frac{a}{k}}\right)\right]^2}\, dx = l.$$

$$(9)$$

Regarding a rigid-bond origami folding joint actuated by a moment M, we only need to resolve integration constants $A, B,$ and C from Eq. 4b-2 and Eq. 4c, details of the computation process is in Supplementary S3. We then find:

$$A = 0, B = -\frac{M}{1+v}, C = 0, F = 0, I = \frac{2a^2 vB}{(1-v)} \sum_{m=1,3,5,\ldots}^{\infty} \left[\frac{1}{m\pi} - \left(\frac{2}{m\pi}\right)^3\right](-1)^{\frac{m-1}{2}} \cos\frac{m\pi y}{2a}.$$

$$(10)$$

Substituting the above integration constants into Eq. 1, we obtain the deflection function for a rigid-bond origami joint under moment, M. When $a \ll l$, the boundary condition in Eq. 4a is also set to be satisfied at the origin ($x = y = 0$). Then, the integration constant I equal to zero and the deflection function is simplified to:

$$w = -\frac{Mx^2}{2D(1-v^2)} + \frac{vMy^2}{2D(1-v^2)} \tag{11}$$

Analogous to that in the transverse force-loaded hinge, we also take the strip at $y = 0$ to compute the deformed position of the edge $x = l'$ under M, which gives

$$\int_0^{l'} \sqrt{1 + \left[\frac{Mx}{D(1-v^2)}\right]^2} \, dx = l \tag{12}$$

To evaluate the accuracy of the analytical model, we calibrate the analytical predictions concerning FEA on two origami folding joints, namely a narrow type sizing 2 mm ×10 mm × 0.125 mm, and a wide type of 10 mm × 2 mm× 0.125 mm. Both hinges are composed of Kapton, whose Young's modulus is 2.5 GPa and Poisson's ratio is 0.34 (49). Referring to the analytical models, the deflections for the narrow and wide origami joints under a terminal force $P = 0.5N$ and $P = 0.005N$ are shown in Fig. 3B(i,iv). Additionally, the deflection under a moment $M = 1N \cdot mm$ and $M = 0.05N \cdot mm$ are also obtained and shown in Fig. 3C(i,iv). It is observed that both hinges bend smoothly to cylindrical surfaces and the loaded panels rotate rigidly to the tangent plane of the deformed hinges.

As a reference, a discretized FEA is used to study the bending of the narrow and wide origami joints. In this and subsequent sections of the paper, the FEA is solved in Abaqus/CAE with geometrical nonlinearity. The settings of the FEA is shown in Supplementary S4. The simulation result for a rigid-bond narrow joint under transverse force is given in Fig. 4A. The deflection on edge $x = l'$ is merely 1.9% lower than that in Fig. 3B(i), which indicates high accuracy of the analytical model. The deviations of deflection on edge $x = l'$ for two origami joints under transverse force and moment are given in Fig. 3B(vii) and Fig. 3C(vii), respectively. In both loading conditions, the deviations increase with deformation. It is observed that the deviations of P-loading converge at 6.5%, while those of M-loading increase dramatically to 55%. The misprediction at a high moment is because the analytical model fails to capture curl deformation. To preserve high accuracy of the model, it is suggested for use when the folding angle is less than 45°. The detailed comparison under varying transverse force and moment are enumerated in Supplementary Fig. S1.

2.2 Semi-rigid bond origami folding joints

In physical origami folding joints, the connection between hinges and panels is normally semi-rigid due to fabrication limitations or properties of the constitutive material. Inspired by the work in (50), we adopt a torsional spring to model this semi-rigid connection, as shown by Fig. 1C. In this section, we model the physical origami folding joints with special focus on the deflection and rotation of hinges. Herein, the hinge is semi-rigidly joined to thick panels on $x = 0, l$, actuated by a transverse force or moment on $x = l$ and free of loads at the remaining two edges $y = \pm a$. Considering the fabrication settings and materials are identical for both material interfaces, we assume that the stiffness of two torsional springs are identical, k_{spr}.
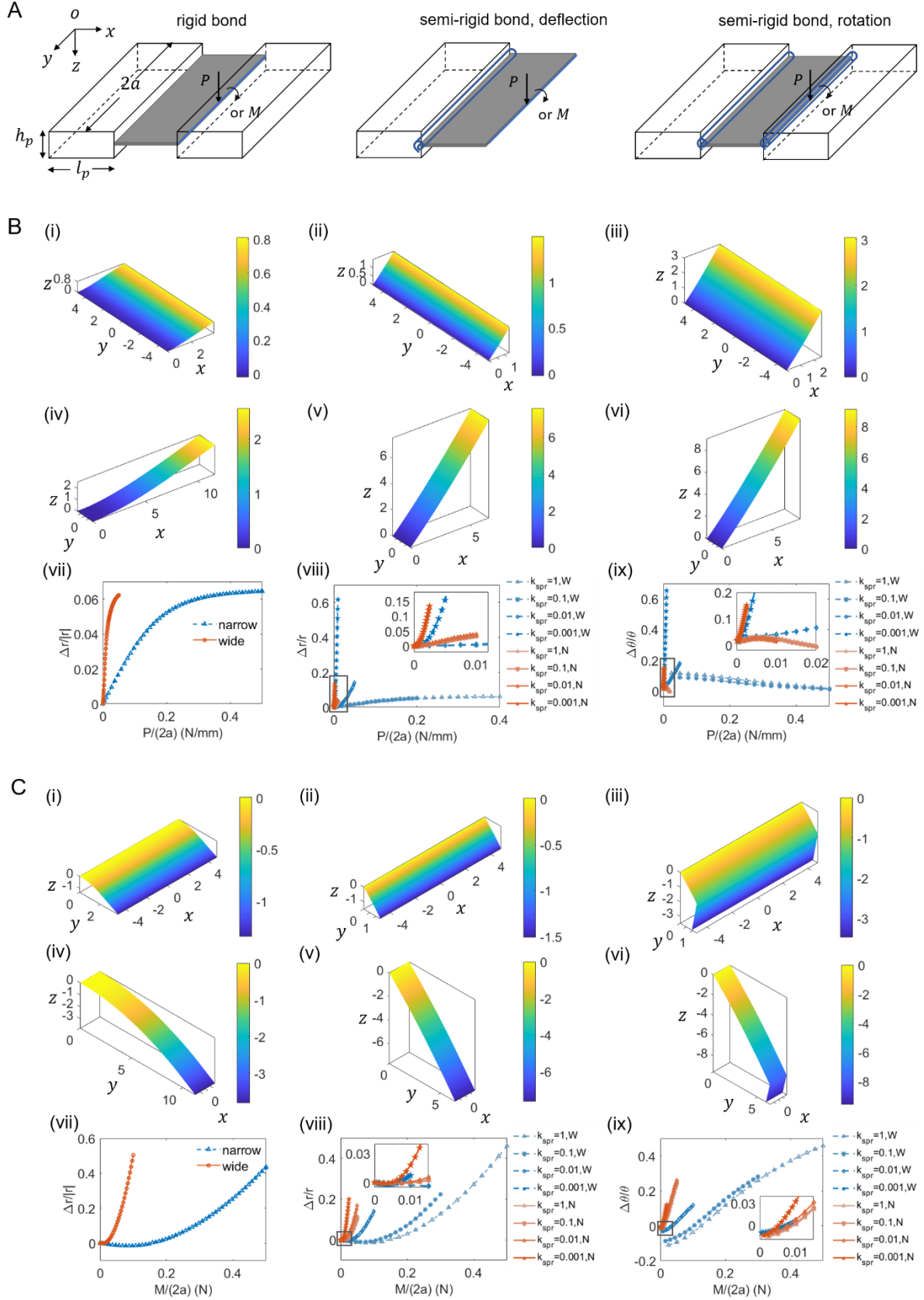
Fig. 3 Comparison of the analytical model and FEA based on two origami folding joints. *Under the boundary conditions in Fig. 3A, the narrow (2×10×0.125 mm³) and wide (10×2×0.125 mm³) origami joints deform to Fig. 3B and Fig. 3C under transverse force and moment, respectively. In each deflection contour, the units of the three axes are millimeters, the fixed left panel ($l_p = 2mm, h_p = 1mm$) is ignored and the right panel is illustrated by its middle plane. Fig. 3B(vii-ix) and C(vii-ix) show the deviations of the analytical model concerning the FE simulation results,* *'N' represents narrow joint, and 'W' is wide type.*

Because the torsional spring merely undergoes rotation, the deflection on edge $x = 0, l$ are zero yet bending moment of hinge equals to the twisting moment of the spring. With incorporation of large deformation, the rotation angle of the torsional springs are $\left(\arctan \varphi_x\right)_{x=0}$, $\left(\theta_{ext} - \arctan \varphi_x\right)_{x=l}$ and their twisting moments are $2ak_{spr}\left(\arctan \varphi_x\right)_{x=0}$, $2ak_{spr}\left(\theta_{ext} - \arctan \varphi_x\right)_{x=l}$, respectively. Herein, θ_{ext} is the folding angle of the loaded panel. Therefore,

$$2ak_{spr}\left(\arctan \varphi_x\right)_{x=0} = \left(\int_{-a}^{a} M_x dy\right)_{x=0}, 2ak_{spr}\left(\theta_{ext} - \arctan \varphi_x\right)_{x=l} = \left(\int_{-a}^{a} M_x dy\right)_{x=l} \tag{13}$$

The boundary and loading conditions for a physical origami folding joint are denoted as follows:

$$w = 0, 2ak_{spr} \arctan \varphi_x = \int_{-a}^{a} M_x dy \quad \text{for } x = 0 \tag{14a}$$

$$2ak_{spr}\left(\theta_{ext} - \arctan \varphi_x\right) = 0, \int_{-a}^{a} Q_x dy = P \quad \text{for } x = l \tag{14b-1}$$

$$2ak_{spr}\left(\theta_{ext} - \arctan \varphi_x\right) = \int_{-a}^{a} Mdy, \int_{-a}^{a} Q_x dy = 0 \quad \text{for } x = l \tag{14b-2}$$

$$M_{xy} = 0 \quad \text{for } y = \pm a \tag{14c}$$

Here, Eq. 14a denotes the deflection and rotation consistency on the elastically supported edge at $x = 0$; Eq. 14b describes the transverse force and moment loading conditions at edge $x = l$; and Eq. 14c indicates no twisting moment is applied to the free edges at $y = \pm a$.

Solving Eq. 14a, Eq. 14b-1, and Eq. 14c with the general form of deflection function w from Eq. 1, bending moment, M_x, twisting moment, M_{xy}, transverse force, Q_x, and bending angle, φ_x from Eq. 3 (details in Supplementary S5), we can obtain the expressions of five integration constants and the folding angle of the loaded panel for a physical origami joint under terminal force P,

$$A = \frac{vP}{2(1+v)}\frac{1}{k \sinh\dfrac{a}{k}}, B = \frac{Pl}{2(1+v)a}, C = \frac{P}{2(1+v)a}, I = \frac{2a^2 vB}{(1-v)}\sum_{m=1,3,5,\dots}^{\infty}\left[\frac{1}{m\pi} - \left(\frac{2}{m\pi}\right)^3\right](-1)^{\frac{m-1}{2}}\cos\frac{m\pi y}{2a}$$
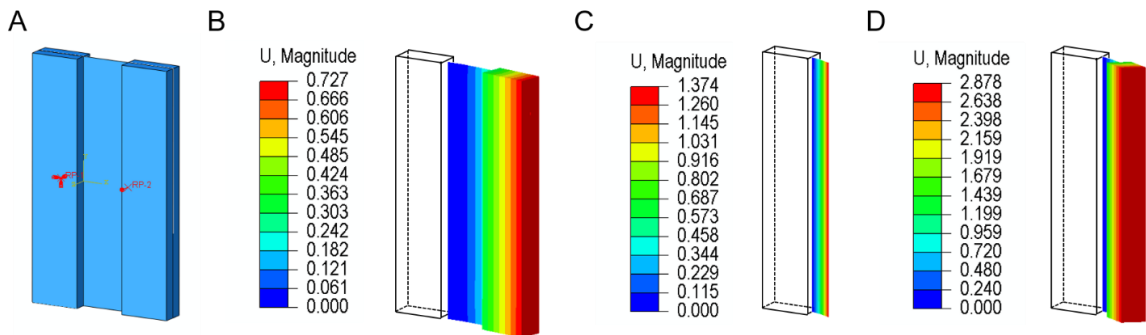
Fig. 4 FEA simulation for a narrow origami pin-joint *(A), which subject to* $P = 0.5N$ *under (B) rigid bonding, (C, D) semi-rigid bond with focus on deflection and rotation. To note,* $k_{spr} = 0.01N / rad$ *for (B-D).*

$$F = \frac{h^2 C}{5(1-v)} - \sum_{m=1,3,5,\ldots}^{\infty} \left\{ \frac{2Cva^2}{1-v}\left[\frac{1}{m\pi} - \left(\frac{2}{m\pi}\right)^3\right] + \frac{4h^2 A}{5m\pi(1-v)}\frac{\cosh\frac{a}{k}}{1+\left(\frac{2a}{km\pi}\right)^2}\right\}(-1)^{\frac{m-1}{2}}\cos\frac{m\pi y}{2a} + \boldsymbol{D}\tan\frac{Pl}{k_{spr}}$$

$$\theta_{ext} = \arctan\left[-\frac{Pl^2}{4a\boldsymbol{D}(1-v^2)} - \tan\frac{Pl}{k_{spr}}\right] \tag{15}$$

A key observation is that the expressions of the integration constants A, B, C and I are identical to those in Eq. 6 and Eq. 7 for a rigid-bond origami joint under terminal force, and the only difference happens in the last term of F. This different term converges to zero if k_{spr} approaches infinity, and the case of infinite k_{spr} is identical to the clamping constraint in rigid-bond prototype. Hence, the rigid-bond origami joint can be viewed as a special case of the semi-rigid prototype.

Similar to the rigid-bond origami joint, the deflection function, $w,$ can also be simplified by taking the constraints in Eq. 14a to be satisfied at the origin when $a \ll l$. Hence, the expressions of deflection function and length preserving constraint become:

$$w = \frac{P}{2a\boldsymbol{D}(1-v^2)}\left[-\frac{x^3}{6} + \frac{lx^2}{2} + \frac{v}{2}(x-l)y^2 + 2k^2 x\left(1 + \frac{av}{k\sinh\frac{a}{k}}\right)\right] + x\tan\frac{Pl}{k_{spr}}$$

$$\int_0^{l'}\sqrt{1 + \left[\frac{P}{2a\boldsymbol{D}(1-v^2)}\left(-\frac{x^2}{2} + lx + 2k^2\left(1 + \frac{av}{k\sinh\frac{a}{k}}\right)\right) + \tan\frac{Pl}{k_{spr}}\right]^2}\,dx = l \tag{16}$$

To solve the deflection function w for a semi-rigid origami joint under moment, M, we apply the five constraints in Eq. 14a, Eq. 14b-2 and Eq. 14c to the general form of deflection function in Eq. 1. The detailed computation process is elaborated in the Supplementary S5 and the five integration constants and folding angle of the loaded panel become:

$$A = 0, B = -\frac{M}{1+v}, C = 0, F = -\boldsymbol{D}\tan\frac{2aM}{k_{spr}}, I = \frac{2a^2 vB}{(1-v)}\sum_{m=1,3,5,\ldots}^{\infty}\left[\frac{1}{m\pi} - \left(\frac{2}{m\pi}\right)^3\right](-1)^{\frac{m-1}{2}}\cos\frac{m\pi y}{2a}$$

$$\theta_{ext} = \arctan\left[\frac{Ml}{\boldsymbol{D}(1-v^2)} + \tan\frac{2aM}{k_{spr}}\right] + \frac{M}{k_{spr}} \tag{17}$$

Comparing the integration constants in Eq. 17 and Eq. 10 also leads to the conclusion that rigid-bond origami joint is also an extreme case of the semi-rigid bond prototype under moment loading condition. Here, the only difference between the two sets of integration constants also happens in F, which converges to zero when k_{spr} approaches infinity. Providing $a \ll l$, the deflection function can also be simplified by simplifying the boundary condition in Eq. 14a, i.e. merely satisfying at the origin. Therefore, the deflection function and deformed position of the right edge are denoted as:

$$w = -\frac{Mx^2}{2D(1-v^2)} + \frac{vMy^2}{2D(1-v^2)} - x\tan\frac{2aM}{k_{spr}}$$

$$\int_0^{l'} \sqrt{1 + \left[\frac{Mx}{D(1-v^2)} + \tan\frac{2aM}{k_{spr}}\right]^2}\, dx = l \qquad (18)$$

Suppose a physical origami folding joint subject to a force eccentric to the folding axis, i.e. $x = r_P, r_P > l$. This loading condition can be equivalent to a distributed force and a moment passing through $x = l$. The efficacy of this equivalent system is verified in Supplementary S6. In this manner, we superpose Eq. 15 and Eq. 17 to compute the deflection function and folding stiffness of an origami folding joint. Herein, the folding stiffness is given by

$$k_{pin} = \frac{P}{\arctan\left[-\dfrac{Pl^2}{4aD(1-v^2)} - \tan\dfrac{Pl}{k_{spr}}\right] + \arctan\left[\dfrac{r_P Pl}{D(1-v^2)} + \tan\dfrac{2ar_P P}{k_{spr}}\right] + \dfrac{r_P P}{k_{spr}}} \qquad (19)$$

Here, the accuracy of the analytical models is also evaluated on the narrow and wide origami folding joints. Considering the flexural rigidity of the Kapton folding hinge is 0.46 N·mm according to Eq. 2, we set k_{spr} equal to 0.01 N/rad and 0.001 N/rad for the narrow and wide origami joints. The deflection surfaces for the narrow folding hinge under transverse force and moment are denoted in Fig. 3B(ii,v) and Fig. 3C(ii,v), respectively. Compared to the rigid-bond origami joints in Fig. 3B(i,iv) and Fig. 3C(i, iv), a key observation is that both hinges tend to behave like rigid panels to rotate along $x = 0$, resulting in more than twice of the deflection. The amplified deflection leads to the conclusion that the mechanical property of the material interface affects the folding stiffness of the origami pin-joints dramatically. The rotation of the right panel for two origami joints are depicted in Fig. 3B(iii,vi) and Fig. 3C(iii,vi), respectively. It is observed that the middle plane of the loaded panel is tangent to or rotated by M / k_{spr} along edge $x = l'$ under transverse force or moment, respectively.

Comparing the FEA in Fig. 4B and the analytical prediction in Fig. 3B(ii), a maximal 8.44% deflection deviation of the deflection on edge $x = l'$ is observed, revealing high accuracy of the analytical model. The full range of deflection deviations on edge $x = l'$ for the physical origami joint under transverse force and moment, are shown in Fig. 3B(viii) and Fig. 3C(viii), respectively. For P-loading, the deviations of the semi-rigid bond are higher than that of the rigid bond prototypes, the main reason is that the proposed analytical model performs better for smaller deformations. Providing the same external force, the folding joint with semi-rigid connection undergoes larger deformation than the rigid bond prototype. While the M-loading shows opposite trend when comparing Fig. 3C(viii) with Fig. 3C(vii), this is due to weakening curled deformation with decreases of k_{spr}. Moreover, the deviations of the analytical model decrease when k_{spr} increases. In Fig. 3B(viii), all deviations, except for those of the narrow origami folding joint with $k_{spr} = 0.001$, are less than 15 %. By comparing Fig. 4B with Fig. 3B(iii), the deviations of θ_{ext} show similar trends as those of the deflection deviations, which also decrease when k_{spr} increase. Without losing accuracy, the analytical model is recommended to simulate origami pin-joints whose folding angles are moderately low, around less than 45°.

The detailed comparison between analytical predictions and FE simulations with varying k_{spr} are shown in Supplementary Fig. S2 and Fig. S3.

3. Experimental calibration of semi-rigid bond

Providing that the semi-rigid connection k_{spr} is given, we can forecast the folding stiffness of physical origami folding joints, as well as the localized bending under transverse force, moment, or hybrid. Therefore, we propose a standard folding test to calibrate k_{spr} of origami joints whose material and fabrication process are predefined. Based on the experimental data, we derive a quantitative model to predict k_{spr} depending on the geometrical and flexible rigidity of folding hinges, so that we can find k_{spr} for origami folding joints with new dimensions and further predict their folding stiffness.

In this work, we prepare various origami folding joints fabricated by the lamination technique (4,18,35), whose structure is denoted Fig. 5A. The holes in Fig. 5A are used for aligning layers of material precisely in the lamination process, and as fixtures to clamp the samples on the test setup (5,22,51). Thereafter, the origami joints undergo repetitive quasi-static folding tests with one panel fixed and the other driven by a step motor. The details of the test are depicted in Supplementary S7. The folding angle over driven force for a joint with $h = 215 \mu m$ and varying l are given in Fig. 5B. Taking an average of $k_{pin} = P / \theta_{ext}$ for repeatable tests and redundant samples, we obtain the folding stiffness for all types of origami pin-joints, given in Fig. 5C. Based on the experimental data, we extract the stiffness of the torsional spring k_{spr} for each type of origami folding joint using Eq. 19, and the results is shown in Fig. 5D. To ensure k_{spr} is scalable with mechanical and geometrical properties of folding hinges,
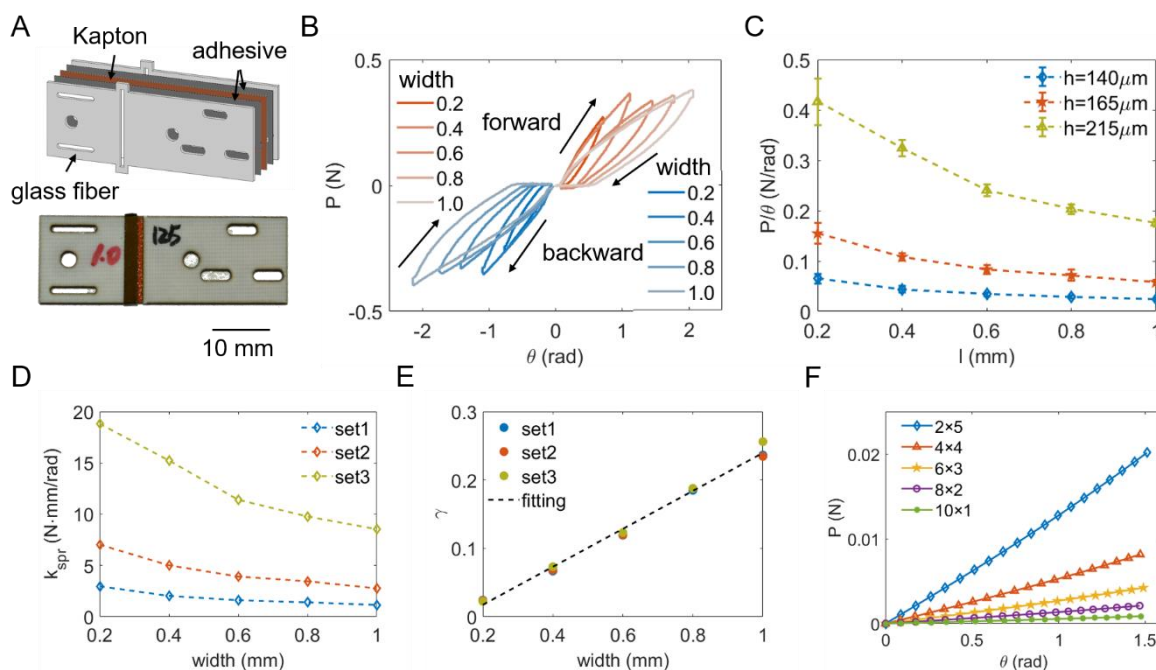
Fig. 5 Experimental results of the semi-rigid connections and predictions on the folding properties of origami joints with varying dimensions. *(A) An origami joint is fabricated by laminate technique. (B) Experimental results for the origami folding joints with $h = 125 \mu m$. Characterized results for (C) folding stiffness, (D) semi-rigid connection, (E) and semi-rigid index. (F) Predictions for physical origami folding joints with varying width l and length a.*

we introduce a semi-rigid index, γ, which is defined by unifying k_{spr} with respect to flexural rigidity, $\boldsymbol{D}$:

$$\gamma = \frac{k_{spr} l^2}{2a\boldsymbol{D}} \tag{20}$$

The semi-rigid index, γ, for three sets of origami pin-joints is shown in Fig. 5E, indicating that γ is linearly related to the width of hinges. By rewriting Eq. 20, we finally achieve the relationship between k_{spr} and $\boldsymbol{D}$ and the geometrical parameters of the hinges,

$$k_{spr} = \frac{2a\boldsymbol{D}}{l}\left(0.2775l - 0.0379\right) \tag{21}$$

With the stiffness of the torsional spring from Eq. 21, the deflection function from Eq. 15 and Eq. 17, and the folding stiffness from Eq. 19, one can successfully predict the mechanical property and localized bending of any origami folding joint fabricated of the same material and by the same approach as denoted in Fig. 5A. As verification, Fig. 5F illustrates the folding angle over driven force curves for five types of origami folding joints with new dimensions, including the narrow and wide types in Fig. 3.

For origami folding joints made from different materials and fabricated by different techniques, we recommend the user to conduct standard folding tests to calibrate the semi-rigid connection on material interfaces, and adopt the proposed analytical model to predict the folding stiffness and localized bending. Providing the basic properties of origami folding joints are known, one can directly integrate them into the modeling framework to accurately predict the mechanics of origami robots.

4. Discussion

Origami folding joints are fundamental components enabling origami robots to achieve mobility and reconfigurability. This paper introduced an analytical model to predict the mechanics of origami folding joints, i.e. localized bending at folding hinges, the semi-rigid, flexible behavior on the material interface, and the folding stiffness of physical origami folding joints. With this analytical model and experimentally characterized semi-rigid connection index, the user can accurately evaluate the folding stiffness of new origami folding joints and the localized bending at the folding hinges under external loads.

This analytical model is, however, not applicable to origami folding joints with thick folding hinges because of the initial thin plate assumption. Referring to the comparison between analytical results and FEA simulations, the deviations increase dramatically when the folding angle is larger than $45°$ under moment loading conditions. Therefore, the proposed analytical model cannot predict the localized deformation of folding hinges when they are fully folded. Moreover, our experiments are conducted on actual prototype of millimeter scale samples. While the model is scalable for other materials and manufacturing processes, for practicality of building a physical prototype, the thickness (h) should be ranges from 50 micrometers to 2 millimeters; the ratio between the thickness (h) and width (l) for folding hinge should be less than 0.2; the stiffness of the hinge material should be higher than 1 MPa.

Extensions and refinements of this work may explore integrating the basic model of folding joints into the framework of origami robot modeling. As scientists and engineers are continuously inspired by origami principles, further engineering of origami structures is

continuing to be developed by replacing creases with folding hinges. Our work lays the foundation for modeling of these engineered origami structures.

Acknowledgements

References

1. D. Rus, C. Sung, Spotlight on origami robots. *Sci. Robot.* **3**, eaat0938 (2018).
2. H. McClintock, F. Z. Temel, N. Doshi, J. S. Koh, R. J. Wood, The milliDelta: A high-bandwidth, high-precision, millimeter-scale Delta robot. *Sci. Robot.* **3**, eaar3018 (2018).
3. S. Felton, M. Tolley, E. Demaine, D. Rus, R. Wood, A method for building self-folding machines. *Science* **345**, 644-646 (2014).
4. R. Niiyama, X. Sun, C. Sung, B. An, D. Rus, S. Kim, Pouch motors, Printable soft actuators integrated with computational design. *Soft Robotics* **2**, 59-70 (2015).
5. A. Firouzeh, J. Paik, Robogami, A fully integrated low-profile robotic origami. *J. Mech. Robot.* **7**, 021009 (2015).
6. J. Li, H. Godaba, Z. Q. Zhang, C. C. Foo, J. Zhu. A soft active origami robot. *Extreme Mech. Lett* **24**, 30-37 (2018).
7. R. J. Lang, *Origami design secrets: mathematical methods for an ancient art. AK Peters/CRC Press* (2011).
8. S. Li, H. Fang, S. Sadeghi, P. Bhovad, K. W. Wang, "Architected origami materials: How folding creates sophisticated mechanical properties." *Adv. Mat.* **31**, 1805282 (2019).
9. M. S. Moses, M. K. Ackerman, G. S. Chirikjian, Origami rotors, Imparting continuous rotation to a moving platform using compliant flexure hinges. *Intl. Design Eng. Tech. Conf. and Comp. and Info. in Eng.* **V06BT07A037** (2013).
10. D. Rus, M. T. Tolley, Design, fabrication and control of origami robots. *Nat. Rev. Mater* **3**, 101 (2018).
11. Y. Chen, R. Peng, Z. You, Origami of thick panels. *Science* **349**, 396-400 (2015).
12. T. Tachi, Simulation of rigid origami. *Origami* **4**, 175-187 (2009).
13. M. Schenk, S. D. Guest, Origami folding, A structural engineering approach. *Origami* **5**, 291-304 (2011).
14. E. T. Filipov, K. Liu, T. Tachi, M. Schenk, G. H.Paulino. Bar and hinge models for scalable analysis of origami. *Int. J. Solids Struct.* **124**, 26-45 (2017).
15. J. S. Dai, J. R. Jones, Kinematics and mobility analysis of carton folds in packing manipulation based on the mechanism equivalent. J. Mech. *Eng. Sci.* **216** 959-970 (2002).
16. S. Sadeghi, S. Li. Dynamic folding of origami by exploiting asymmetric bi-stability. *Extreme Mech. Lett* **40**, 100958 (2020).
17. S. Li, D. M. Vogt, D. Rus, R. J. Wood, Fluid-driven origami-inspired artificial muscles. *Proc. Natl. Acad. Sci.* **114**, 13132-13137 (2017).
18. S. Russo, T. Ranzani, C. J. Walsh, R. J. Wood, An Additive Millimeter-Scale Fabrication Method for Soft Biocompatible Actuators and Sensors. *Adv. Mat. Tech.* **2**, 1700135 (2017).
19. H. Yang, B. S. Yeow, Z. Li, K. Li, T. H. Chang, L. Jing, Y. Li, J. S. Ho, H. Ren, P. Y. Chen, Multifunctional metallic backbones for origami robotics with strain sensing and wireless communication capabilities. *Sci. Robot.* **4**, eaax7020 (2019).
20. Y. Kim, H. Yuk, R. Zhao, S. A. Chester, X. Zhao, Printing ferromagnetic domains for untethered fast-transforming soft materials. *Nature* **558**, 274 (2018).
21. A. C. Siegel, S. T. Phillips, M. D. Dickey, N. Lu, Z. Suo, G. M. Whitesides, Foldable printed circuit boards on paper substrates. *Adv. Funct. Mat.* **20**, 28-35 (2010).

22. M. Salerno, F. Zuliani, A. Firouzeh, J. Paik, Design and control of a low profile electromagnetic actuator for foldable pop-up mechanisms. *Sens. Actuators A, Phys.* **265**, 70-78 (2017).
23. K. Zhang, C. Qiu, J. S. Dai, An extensible continuum robot with integrated origami parallel modules. *J. Mech. Robot.* **8**, 031010 (2016).
24. J. Rogers, Y. Huang, O. G. Schmidt, D. H. Gracias, Origami mems and nems. *Mrs Bulletin* **41**, 123-129 (2016).
25. Y. Shi, F. Zhang, K. Nan, X. Wang, J. Wang, Y. Zhang, H. Luan, K.-C. Hwang, Y. Huang, J. A. Rogers. Plasticity-induced origami for assembly of three dimensional metallic structures guided by compressive buckling. *Extreme Mech. Lett* **11**, 105-110 (2017).
26. J. A. Faber, A. F. Arrieta, A. R. Studart, Bioinspired spring origami. *Science* **359**, 1386-1391 (2018).
27. H. Fang, K. W. Wang, S. Li. Asymmetric energy barrier and mechanical diode effect from folding multi-stable stacked-origami. *Extreme Mech. Lett* **17**, 7-15 (2017).
28. M. Schenk, S. D. Guest, Geometry of Miura-folded metamaterials. *Proc. Natl. Acad. Sci.* **110**, 3276-3281 (2013).
29. Z. Zhang, B. Luce, C. Ma, B. Xie, N. Hu. Programmable origami-inspired cellular architected building blocks for flow-regulating adaptive weir. *Extreme Mech. Lett*, 100974 (2020).
30. E. T. Filipov, T. Tachi, G. H. Paulino, Origami tubes assembled into stiff, yet reconfigurable structures and metamaterials. *Proc. Natl. Acad. Sci.* **112**, 12321-12326 (2015).
31. J. T. Overvelde, J. C. Weaver, C. Hoberman, K. Bertoldi, Rational design of reconfigurable prismatic architected materials. *Nature* **541**, 347 (2017).
32. M. Eidini. Zigzag-base folded sheet cellular mechanical metamaterials. *Extreme Mech. Lett* **6**, 96-102 (2016).
33. H. Vandeparre, Q. Liu, I. R. Minev, Z. Suo, S. P. Lacour, Localization of folds and cracks in thin metal films coated on flexible elastomer foams. *Adv. Mat.* **25**, 3117-3121 (2013).
34. S. Miyashita, S. Guitron, M. Ludersdorfer, C. R. Sung, D. Rus, An untethered miniature origami robot that self-folds, walks, swims, and degrades. *ICRA*, 1490-1496 (2015).
35. B. An, S. Miyashita, M. T. Tolley, D. M. Aukes, L. Meeker, E. D. Demaine, D. Rus, An end-to-end approach to making self-folded 3D surface shapes by uniform heating. *ICRA*, 1466-1473 (2014).
36. X. Guo, H. Li, B. Y. Ahn, E. B. Duoss, K. J.Hsia, J. A. Lewis, and Ralph G. Nuzzo, "Two-and three-dimensional folding of thin film single-crystalline silicon for photovoltaic power applications." *Proc. Natl. Acad. Sci.* **106**, 20149-20154 (2009).
37. Q. Ge, C. K. Dunn, H. J. Qi, M. L. Dunn, Active origami by 4D printing. *Smart Mat. Struct.* **23**, 094007 (2014).
38. Y. Liu, J. K. Boyles, J. Genzer, M. D. Dickey, Self-folding of polymer sheets using local light absorption. *Soft matter* **8**, 1764-1769 (2012).
39. J. H. Na, A. A. Evans, J. Bae, M. C. Chiappelli, C. D. Santangelo, R. J. Lang, R. C. Hayward, Programming reversibly self-folding origami with micropatterned photo-crosslinkable polymer trilayers. *Adv. Mat.* **27**, 79-85 (2015).
40. Q. Zhang, J. Wommer, C. O'Rourke, J. Teitelman, Y. Tang, J. Robison, G. Lin, J. Yin. Origami and kirigami inspired self-folding for programming three-dimensional shape shifting of polymer sheets with light. *Extreme Mech. Lett* **11**, 111-120 (2017).
41. I. L. Delimont, S. P. Magleby, L. L. Howell, Evaluating compliant hinge geometries for origami-inspired mechanisms. *Journal of Mechanisms and Robotics* **7**, 011009 (2015).
42. Y. Hongying, G. Zhen, Z. Di, L. Peng. Mechanical Characteristics of Origami Mechanism Based on Thin Plate Bending Theory. *J. Applied Mech.* **86**, 081008 (2019).
43. E. A. P. Hernandez, D. J. Hartl, E. Akleman, D. C. Lagoudas, Modeling and analysis of origami structures with smooth folds. *Computer-Aided Design* **78**, 93-106 (2016).
44. B. Y. Ahn, D. Shoji, C. J. Hansen, E. Hong, D. C.Dunand, J. A. Lewis, Printed origami structures. *Adv. Mat.* **22**, 2251-2254 (2010).
45. T. J. Hughes, W. K. Liu, Nonlinear finite element analysis of shells, Part I. Three-dimensional shells. *Computer methods in applied mech. eng.* **26**, 331-362 (1981).
46. S. P. Timoshenko, S. Woinowsky-Krieger, Theory of plates and shells. *McGraw-hill* (1959).
47. C. R. Calladine, Theory of Shell Structures. *Cambridge University Press* (1989)
48. E. Reissner, On bending of elastic plates. *Quarterly of Applied Mathematics* **5**, 55-68 (1947).

49. W. He, P. Goudeau, E. Le Bourhis, P. O. Renault, J. C. Dupré, P. Doumalin, S. Wang Study on Young's modulus of thin films on Kapton by microtensile testing combined with dual DIC system. *Surf. Coat. Technol.* **308**, 273-279 (2016).
50. S. L. Chan, P. T. Chui, Non-linear static and cyclic analysis of steel frames with semi-rigid connections. *Elsevier* (2000).
51. Z. Zhakypov, K. Mori, K. Hosoda, J. Paik, Designing minimal and scalable insect-inspired multi-locomotion millirobots. *Nature* **571**, 381-386 (2019).
52. ASTM International *Standard Test Method for Tensile Properties of Plastics. ASTM D638-14*. ASTM International, 2015.